Engineering Fracture Mechanics 343 (2026) 112277

Contents lists available at ScienceDirect

Engineering Fracture Mechanics

journal homepage: www.elsevier.com/locate/engfracmech

Constitutive and fracture behaviour of additively manufactured aluminium

Jingsheng Zhou [a], Ruizhi Zhang [a,*], Mohsen Amraei [b], Leroy Gardner [a]

[a] Department of Civil and Environmental Engineering, Imperial College London, London, UK
[b] Department of Mechanical and Materials Engineering, University of Turku, Turku, Finland

A R T I C L E I N F O

Keywords:
Additive manufacturing
Aluminium
Powder bed fusion
Fracture
Constitutive property

A B S T R A C T

This paper presents a detailed experimental and numerical study into the constitutive and fracture behaviour of additively manufactured AlSi10Mg aluminium alloy produced by laser beam powder bed fusion (PBF-LB/M). A series of 26 coupons with various geometries (to achieve a range of stress states) and build directions ($\theta = 0^{\circ}$, 45° and 90° relative to the layer direction, to investigate anisotropy) were additively manufactured and tested. The PBF-LB/M AlSi10Mg material showed mild constitutive anisotropy, with the highest Young's modulus and proof strengths observed for the 0° coupons. For the case of smooth round bars, an appreciable discrepancy in engineering fracture strain was observed between repeated tests on the 90° coupons, with up to almost 60% differences, indicating potential variability in defect density. Complementary finite element models were developed to extract fracture strains and stress states. The analysis showed minor anisotropy in the fracture properties, with two outliers in the 90° coupons that exhibited considerably higher fracture strains than the 0° coupons, attributed to good interlayer adhesion and a reduced defect density near the critical cross-section. Two ductile fracture criteria, namely the Positive Stress Triaxiality-Lode Angle Parameter Interaction Model (PTLIM) and the Lode angle Modified Void Growth Model (LMVGM), were calibrated against the test data and shown to achieve comparable predictive capabilities.

1. Introduction

In recent years, several metal additive manufacturing (AM) techniques have gained significant attention due to their ability to readily fabricate complex components and to enable the efficient use of high-performance materials in advanced engineering applications [1,2]. These AM techniques have shown great potential for applications in both structural and aerospace engineering, such as for the fabrication of lightweight lattice components [3], optimised load-carrying structural elements [1,4–6] and hybrid AM–hot-rolled steel components [7,8].

Laser beam powder bed fusion (PBF-LB/M) is a metal AM process capable of producing geometrically complex, highly optimised structures with high dimensional accuracy, though generally at slower deposition rates than wire-based methods such as Wire Arc Additive Manufacturing (WAAM). The PBF-LB/M process involves the layer-by-layer deposition of metal powder, featuring selective melting and rapid solidification at predetermined locations using a laser beam. In previous studies of PBF-LB/M stainless steels [9,10], distinctly different mechanical responses were observed compared with those of traditionally manufactured stainless steels.

* Corresponding author.
E-mail address: ruizhi.zhang@imperial.ac.uk (R. Zhang).

https://doi.org/10.1016/j.engfracmech.2026.112277
Received 2 February 2026; Received in revised form 19 March 2026; Accepted 13 May 2026
Available online 17 May 2026

Anisotropic plasticity and fracture behaviour under various stress states were also observed. Similar anisotropic plastic behaviour has been reported in PBF-LB/M aluminium alloys [11]; however, studies into their fracture properties remain limited. As a lightweight, high-performance material, aluminium lends itself particularly well to the emerging opportunities offered by additive manufacturing, especially in aerospace and automotive applications, but also increasingly in construction. Previous studies have reported that the mechanical properties of PBF-LB/M aluminium are comparable to or superior to those of their cast and wrought counterparts [12,13]. However, PBF-LB/M aluminium alloy often exhibits a certain level of anisotropy in strength and ductility, attributed to its cellular microstructure, crystallographic texture and melt pool boundaries (MPBs), as well as other features such as defects arising from the fabrication process [14,15]. Coupons tested perpendicular to the build direction have been generally found to exhibit higher tensile strength and ductility than those tested parallel to the build direction [11]. Anisotropic fracture characteristics have been also reported for PBF-LB/M aluminium alloy. Coupons loaded parallel to the build direction have exhibited crack propagation preferentially along the MPBs [16], whereas, for those loaded perpendicular to the build direction have shown fracture paths involving a combination of propagation across melt pools and along the MPBs [14,15]. Such anisotropy in strength, ductility and fracture characteristics, though not apparent in some studies [16,17], can be mitigated by subsequent heat treatment, albeit typically at the expense of strength [18]. Considerable efforts have been also dedicated to the behaviour [13,19] and optimisation [20,21] of structural elements produced by PBF-LB/M, with the aim of elucidating the influence of process parameters on overall structural performance and harnessing the unique capabilities of AM to create complex geometries that were previously constrained by the manufacturability limitations of conventional formative and subtractive manufacturing techniques.

Despite recent advances in additive manufacturing, limited research has addressed the fracture behaviour of aluminium alloys produced by PBF-LB/M. To bridge this gap, this paper investigates the constitutive and fracture behaviour of the AlSi10Mg aluminium alloy produced by PBF-LB/M via experimental and numerical analyses. A comprehensive test series comprising 26 coupons with different build orientation angles was conducted under various stress states. Additionally, parallel FE models were developed to examine and characterise the influence of stress state and build direction on the fracture behaviour.

2. Experimental programme

2.1. Material and specimens

A total of 26 coupons were manufactured using an SLM 280 HL twin metal printer, featuring a 280 mm × 280 mm × 365 mm building chamber and two Yb-fibre lasers, in the Department of Mechanical and Materials Engineering at the University of Turku. During the PBF-LB/M process, successive layers of metal powder were spread by a recoater and selectively melted by high-energy laser beams and solidified at predefined locations based on a 3D digital model. All PBF-LB/M process parameters used in this study are the same as those in [13], as summarised in Table 1. A bi-directional stripe scanning strategy with a 67° interlayer rotation was employed during fabrication to minimise residual stresses and distortions.

All specimens were built using AlSi10Mg powder at a deposition rate of 29.8 cm^3/hour; the nominal chemical composition and mechanical properties of the PBF-LB/M AlSi10Mg material can be found in [13]. The coupon layout is shown in Fig. 1, where the coupons were printed at 0°, 45° and 90° relative to the build plate (i.e. $\theta = 0°$, 45° and 90°, where θ is the angle between the longitudinal axis of the coupon and the deposition layers, as shown in Fig. 1(b)). A spacing of approximately 15 mm was maintained between coupons to prevent spatter, local overheating and distortion during the PBF-LB/M process. Support structures were fabricated to secure the specimens during printing and to minimise distortion upon build plate removal. After printing, all specimens were removed from the build plate using a bandsaw.

Nine coupons with different geometries and build direction angles were loaded in monotonic tension to investigate their constitutive and fracture properties. Among these, a standard smooth round bar (SRB) coupon, which was designed to generate a uniaxial stress state (stress triaxiality η of 1/3 and Lode angle parameter ξ of 1) based on EN ISO 6892–1 [22], was tested to obtain the constitutive response and the plastic strain at fracture initiation ε_f (referred to as the fracture strain), as shown in Fig. 2(a). The stress triaxiality η is defined by the first invariant of the stress tensor I_1 and the second invariant of the deviatoric stress tensor J_2, as expressed by:

$$\eta = \frac{I_1}{3\sqrt{3J_2}} = \frac{\sigma_h}{\sigma_{eq}} \tag{1}$$

where $\sigma_h = I_1/3$ is the hydrostatic stress, $\sigma_{eq} = \sqrt{3J_2}$ is the equivalent von Mises stress. The value of η can also be expressed as the ratio of the mean stress to the equivalent von Mises stress, even for an anisotropic material [23]. The Lode angle parameter ξ is defined as:

Table 1
PBF-LB/M processing parameters.

Laser power (W)	Laser spot diameter (µm)	Scannig speed (mm/s)	Layer thickness (µm)	Hatch distance (µm)	Scanning rotation (°)	Preheated powder bed (°C)	Shielding gas
370	80	1150	30	120	67	150	Argon

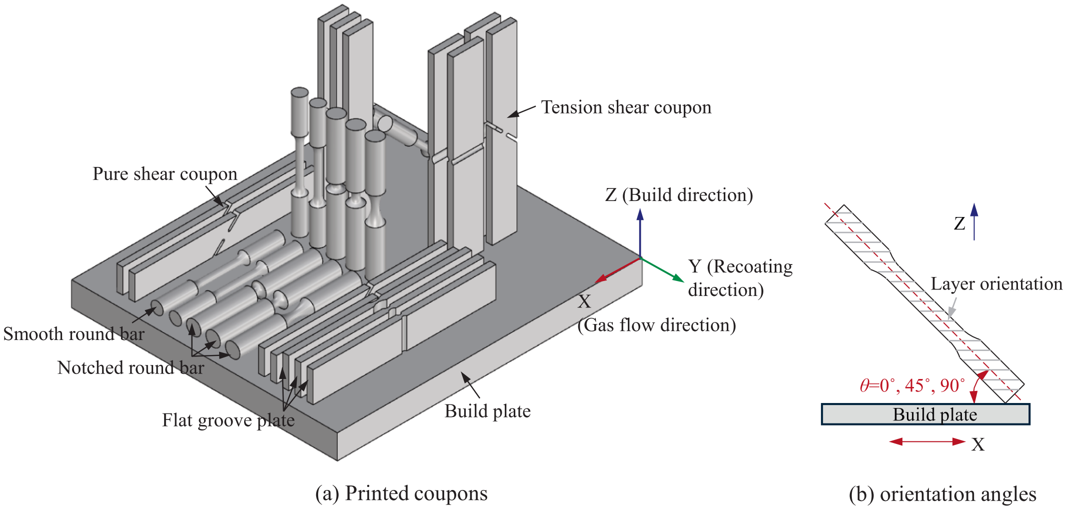

Fig. 1. Schematic illustration of printed coupons and coupon orientation angles.

$$\xi = \frac{27}{2}\frac{J_3}{(3J_2)^{3/2}} \tag{2}$$

where J_3 is the third invariant of the deviatoric stress tensor. Three build orientation angles ($\theta = 0^\circ$, 45° and 90°) were considered for the smooth round bar coupons in order to enable the calibration of the three-dimensional anisotropic yield criterion presented in [23]. Two repeated coupon tests were conducted for each build direction angle.

The remaining coupons were designed to obtain the fracture properties only, and each printed at $\theta = 0^\circ$ and $\theta = 90^\circ$. Three configurations of notched round bar (NRB) coupons were designed to obtain the fracture strains at high triaxial stress states, i.e. $\eta > 1/3$ and $\xi = 1$, with different notch radii used to achieve varying levels of stress triaxiality. Theoretically, specimens with larger notch radii experience larger values of the second and third principal stresses, resulting in higher values of stress triaxiality [24]. Accordingly, three NRBs were designed with radii of 3.5 mm, 6 mm and 20 mm, referred to as NRB-R3.5, NRB-R6 and NRB-R20, respectively, as shown in Fig. 2(b).

Similarly, three configurations of grooved plate (GP) specimens were designed to achieve a plane strain condition, which theoretically corresponds to a ξ value of 0 in the plastic range for incompressible materials [24]. As with the NRB specimens, the η value in GP specimens increases with the notch radius and is larger than 1/3. Three GP specimens were designed with radii of 2 mm, 4 mm and 10 mm, referred to as GP-R2, GP-R4 and GP-R10, respectively, as shown in Fig. 2(c).

Pure shear (PS) specimens were designed to investigate the fracture strains under low values of both stress triaxiality and Lode angle parameter, while tension shear (TS) specimens were designed to investigate the fracture strains under moderate η and ξ values. Both specimen types have similar geometry but different angles between the minimum cross-section and the loading direction: 0° for the PS specimens and 45° for the TS specimens, as shown in Fig. 2(d, e). Two bolt holes were designed on both sides of the coupons to fit pin supports, following the recommendations in [24] to release appreciable tensile stresses that can otherwise arise at large deformations. Two repeated tests were performed for each PS and TS coupon type and build direction angle.

The coupon identifiers follow the format "Coupon-θ", where "-1" or "-2" is added at the end if repeated tests were performed. For example, the second repeated test of the PS specimen at $\theta = 90^\circ$ is referred to as PS-90–2. The measured geometries of each coupon are reported in Table 2, including the diameter of the SRB coupons in the parallel length d_{SRB}, the minimum diameter of the NRB coupons d_{NRB}, the notch radius of the NRB coupons R_{NRB}, the minimum thickness of the GP coupons t_{GP}, the notch radius of the GP coupons R_{GP}, the width of the GP coupons W_{GP}, the width of the notched region for the PS W_{PS} and TS W_{TS} coupons and the minimum thickness of the notched region for the PS t_{PS} and TS t_{TS} coupons.

The average density of the printed material was determined to be 2.58 g/cm^3 based on Archimedes' measurements, which is slightly lower than the value provided in the material data sheet, i.e. 2.67 g/cm^3. The lower density may be attributed to internal defects, such as pores and micro-cracks.

2.2. Test setup

An Instron 5984 150 kN universal testing machine was used to apply the loads to the coupon specimens, as shown in Fig. 3. Two pairs of two-camera StrainMaster Digital Image Correlation (DIC) systems were used to capture the surface deformations and strains on both the front and rear faces of each coupon. Random white speckles were sprayed onto the specimen surfaces over a black background for the DIC measurements. A similar test setup was adopted in [25]. The cameras were first calibrated using a stereo calibration board, and the grid of markers on the calibration board was automatically detected using the DaVis 10 software [26], which maps the pixel

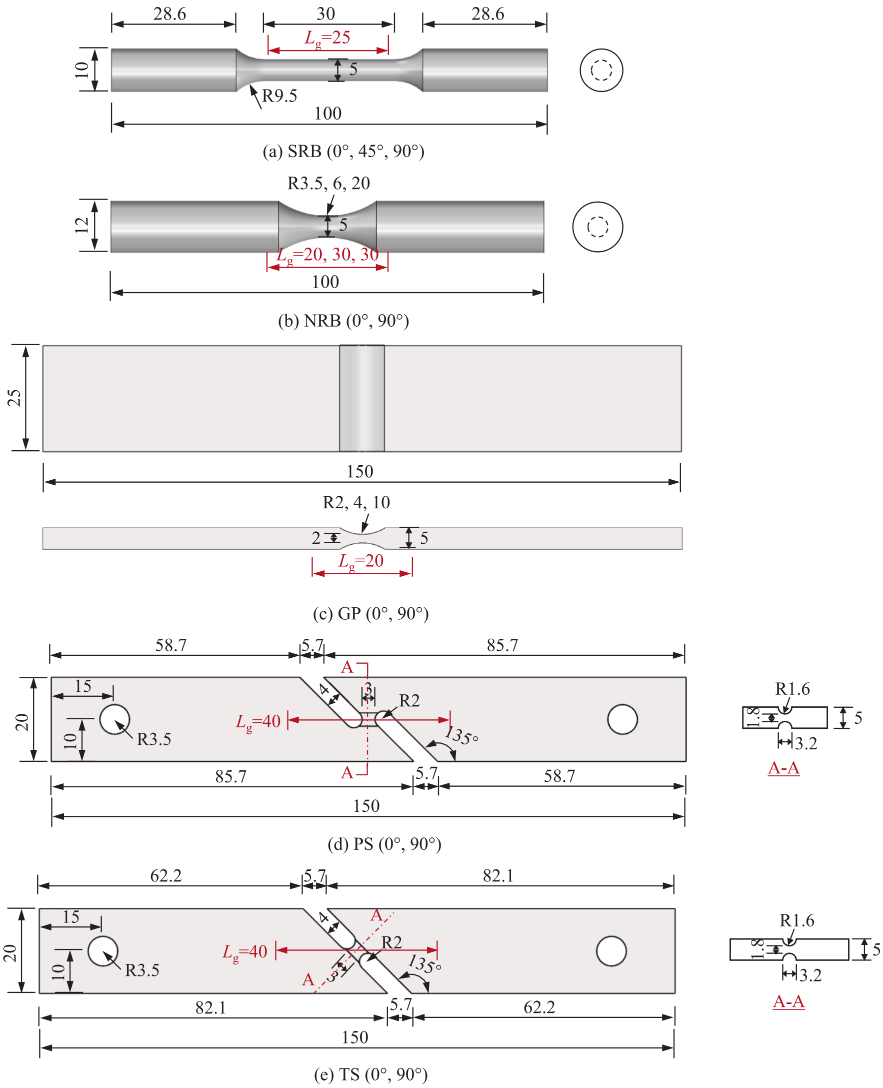

Fig. 2. Nominal geometry of tested coupons (mm).

data to real coordinates. All specimens, except for the PS and TS coupons, were directly clamped between the machine jaws, as shown in Fig. 3(a). For the PS and TS coupons, two pin supports were designed, as shown in Fig. 3(b), providing a pinned boundary condition that allows free rotations of the central region of the coupons and relieves additional transverse tension, thereby maintaining a relatively constant stress state at the critical cross-section throughout the loading history. The applied load was recorded using a built-in load cell in the testing machine. Both the load and DIC images were synchronously recorded at 1 s intervals and post-processed using the DaVis 10 software.

2.3. Test results

2.3.1. Coupons for investigating constitutive behaviour (SRB)

Different gauge lengths L_g were employed for the different coupon types, as summarised in Table 2 and indicated in Fig. 2. For the SRB specimens, a gauge length L_g of 25 mm was chosen, which corresponds to $5.65\sqrt{A}$ [22], where A is the cross-sectional area of the coupon within the parallel length. The engineering stress–strain curves for all SRBs are shown in Fig. 4. These curves were derived using the measured geometries and gauge lengths given in Table 2. Table 3 presents the key mechanical properties obtained from all SRB specimens, including the Young's modulus E, Poisson's ratio ν, 0.2% proof strength $\sigma_{0.2}$, 1.0% proof strength $\sigma_{1.0}$, 2.0% proof strength $\sigma_{2.0}$, ultimate strength σ_u, strain at ultimate strength ε_u, engineering strain at fracture ε_{ef} and the parameters n [27] and m [28,29] from the two-stage Ramberg-Osgood material model. The Young's modulus E was calculated as the slope of the linear portion of the stress–strain curve, specifically between approximately $0.25\sigma_{0.2}$ and $0.35\sigma_{0.2}$ [30]. The Poisson's ratio ν was determined as the ratio of the mean transverse to mean longitudinal strains within the same range. For the SRB specimens, the transverse strain can be

Table 2
Measurements of key features of each coupon (mm).

Coupon	Diameter/Width	Thickness	Notch radius	Gauge length
SRB-0–1	$d_{SRB} = 4.91$	—	—	25
SRB-0–2	$d_{SRB} = 4.96$	—	—	25
SRB-45–1	$d_{SRB} = 4.99$	—	—	25
SRB-45–2	$d_{SRB} = 4.98$	—	—	25
SRB-90–1	$d_{SRB} = 4.91$	—	—	25
SRB-90–2	$d_{SRB} = 4.97$	—	—	25
NRB-R3.5–0	$d_{NRB} = 4.88$	—	$R_{NRB} = 3.38$	20
NRB-R3.5–90	$d_{NRB} = 4.88$	—	$R_{NRB} = 3.30$	20
NRB-R6-0	$d_{NRB} = 4.84$	—	$R_{NRB} = 5.95$	20
NRB-R6-90	$d_{NRB} = 4.84$	—	$R_{NRB} = 5.95$	20
NRB-R20-0	$d_{NRB} = 4.91$	—	$R_{NRB} = 20.40$	30
NRB-R20-90	$d_{NRB} = 4.90$	—	$R_{NRB} = 20.20$	30
GP-R2-0	$W_{GP} = 25.46$	$t_{GP} = 2.09$	$R_{GP} = 1.85$	20
GP-R2-90	$W_{GP} = 25.02$	$t_{GP} = 2.04$	$R_{GP} = 2.02$	20
GP-R4-0	$W_{GP} = 25.51$	$t_{GP} = 1.98$	$R_{GP} = 3.96$	20
GP-R4-90	$W_{GP} = 25.06$	$t_{GP} = 1.95$	$R_{GP} = 3.92$	20
GP-R10-0	$W_{GP} = 25.56$	$t_{GP} = 1.99$	$R_{GP} = 10.02$	20
GP-R10-90	$W_{GP} = 25.04$	$t_{GP} = 1.98$	$R_{GP} = 9.93$	20
PS-0–1	$W_{PS} = 2.96$	$t_{PS} = 1.85$	—	40
PS-0–2	$W_{PS} = 2.99$	$t_{PS} = 1.79$	—	40
PS-90–1	$W_{PS} = 2.99$	$t_{PS} = 1.75$	—	40
PS-90–2	$W_{PS} = 2.92$	$t_{PS} = 1.81$	—	40
TS-0–1	$W_{TS} = 2.98$	$t_{TS} = 1.79$	—	40
TS-0–2	$W_{TS} = 2.96$	$t_{TS} = 1.78$	—	40
TS-90–1	$W_{TS} = 2.97$	$t_{TS} = 1.78$	—	40
TS-90–2	$W_{TS} = 2.97$	$t_{TS} = 1.77$	—	40

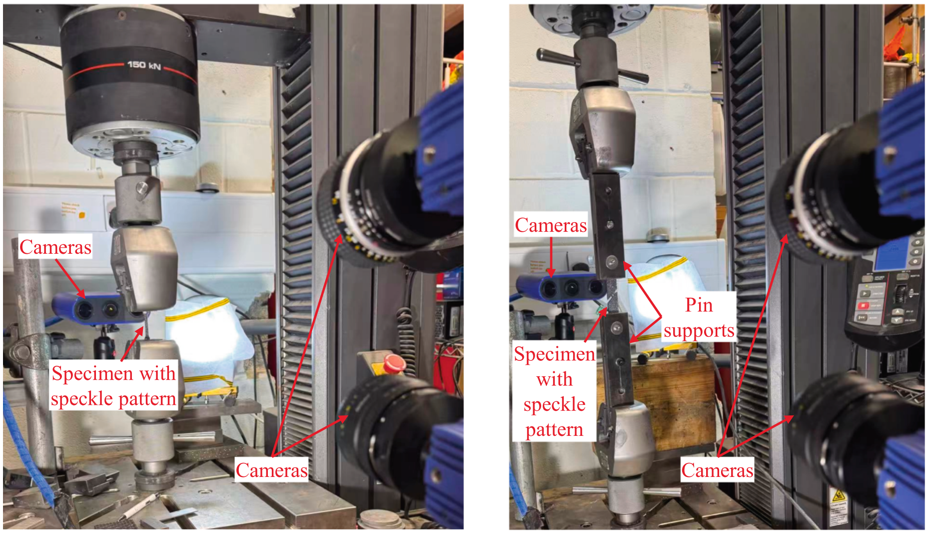

(a) Test setup for SRB, NRB, and GP (b) Test setup for PS and TS

Fig. 3. Test setup for coupon specimens.

determined based on the change in specimen diameter. However, the 3D DIC system is not able to capture the deformation of the entire specimen due to the camera views being partially obstructed by the specimen itself, as shown in Fig. 5(a). The transverse strain $\varepsilon_{\mathrm{tran}}$ was therefore calculated from Eq. (3):

$$\varepsilon_{\mathrm{tran}} = \frac{dR_{\mathrm{SRB}}}{R_{\mathrm{SRB}}} = \frac{2\pi R_{\mathrm{SRB}}\theta_{\mathrm{r}} - 2\pi(R_{\mathrm{SRB}} - dR_{\mathrm{SRB}})\theta_{\mathrm{r}}}{2\pi R_{\mathrm{SRB}}\theta_{\mathrm{r}}} = \frac{L_{\mathrm{SRB}} - l_{\mathrm{SRB}}}{L_{\mathrm{SRB}}} \tag{3}$$

in which θ_{r}, R_{SRB}, dR_{SRB}, L_{SRB} and l_{SRB} are defined in Fig. 5(b).

Fig. 6 shows histograms with error bars representing the standard deviation of the measured 0.2% proof (yield) and ultimate strengths and engineering fracture strains for specimens in all three printing directions. Mild anisotropic constitutive behaviour is observed, with the highest strain hardening found in the SRB-90 specimens; this is consistent with the finding presented in [13]. The

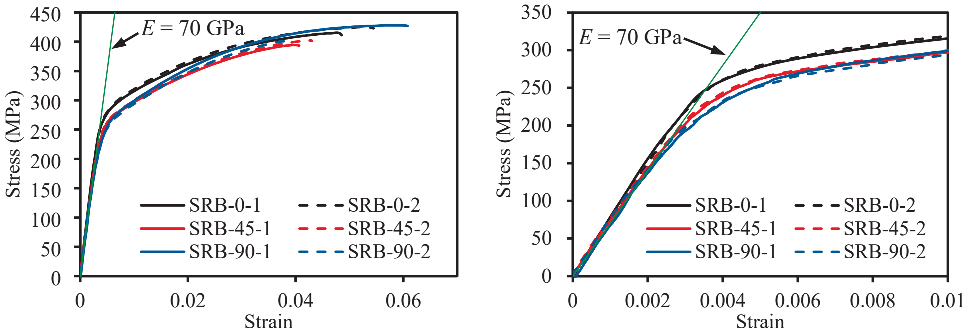

(a) Full range (b) Initial range up to 1% strain

Fig. 4. Engineering stress–strain curves from all SRBs.

Table 3
Key mechanical properties from SRBs.

Coupon	E (MPa)	ν	$\sigma_{0.2}$ (MPa)	$\sigma_{1.0}$ (MPa)	$\sigma_{2.0}$ (MPa)	σ_u (MPa)	ε_u(%)	ε_{ef}(%)	n	m
SRB-0–1	78,330	0.306	282.0	336.8	373.6	415.4	4.77	4.79	10.5	2.5
SRB-0–2	74,310	0.318	288.3	341.8	379.0	425.0	5.29	5.29	9.9	3.0
SRB-45–1	68,240	0.287	273.0	319.4	361.7	394.4	4.04	4.07	10.5	2.2
SRB-45–2	70,160	0.309	273.6	321.3	364.8	402.3	4.19	4.31	11.6	2.3
SRB-90–1	70,500	0.306	265.8	326.4	376.5	427.9	5.91	6.08	7.8	3.4
SRB-90–2	70,010	0.292	263.9	322.0	368.9	400.7	3.74	3.81	8.5	1.8

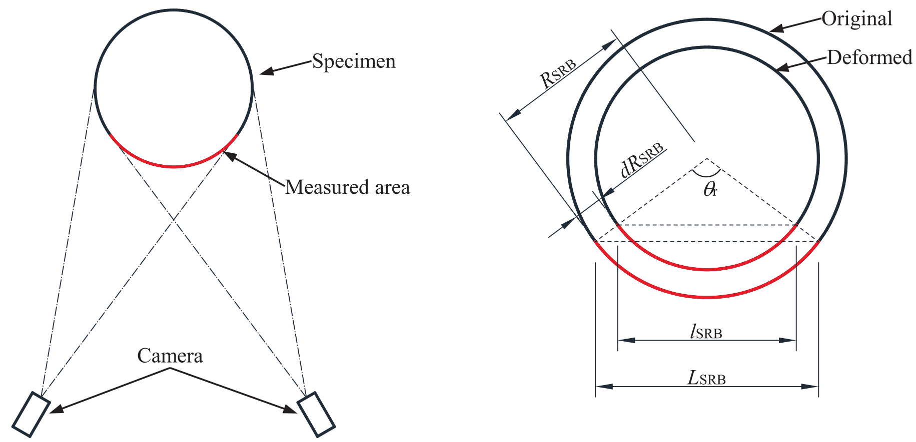

(a) Schematic of DIC measured area (b) Schematic of cross-section

Fig. 5. Schematic illustration of calculation of Poisson's ratio.

maximum Young's modulus and proof strengths occur at $\theta = 0°$, which is associated with the texture and elongated grains relative to the loading direction, as reported in previous studies on PBF-LB/M aluminium alloy [15,31,32]. The measured engineering fracture strains ranged from 4% to 6%, indicating limited ductility, typical of PBF-LB/M aluminium alloys.

The SRB-90 specimens exhibit relatively large scatter in both ultimate strength and engineering fracture strain, as reflected by the standard deviations in Fig. 6. This scatter may be related to variations in interlayer defects, which have a more direct influence on the macroscopic mechanical response when deposition layers are perpendicular to the loading direction, i.e. θ =90°. The variation in engineering fracture strain can be explained in terms of ductile fracture mechanisms. Based on void growth and coalescence theory [24,33,34], fracture initiates once the adjacent voids coalesce as a result of the continuous growth of voids under plastic deformation. A higher defect density reduces the spacing between voids and promotes localised stress concentrations, thereby facilitating earlier fracture initiation.

Fig. 7 shows the fracture profiles of each specimen. The fracture profiles of the PBF-LB/M specimens indicate contributions from both inclusions and manufacturing defects. Fracture surfaces oriented near 45° are observed in both SRB-45 specimens, aligning with the deposition direction, as shown in Fig. 7(b). This is attributed to a higher density of defects (pores and micro-cracks) between

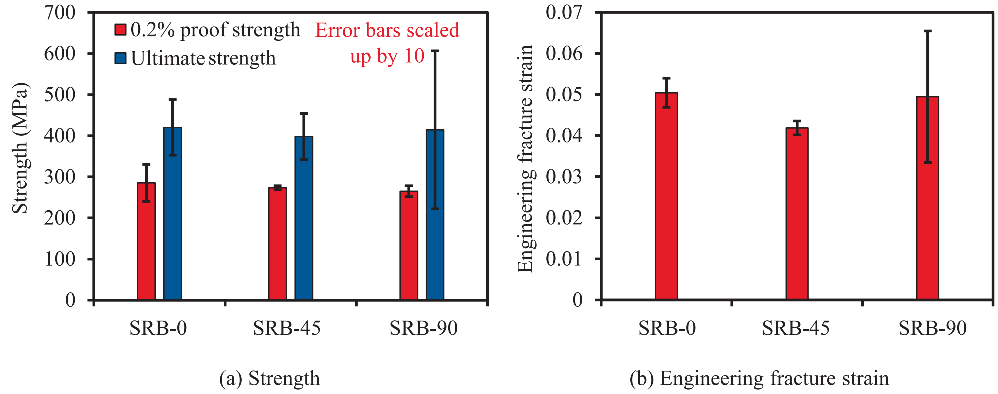

Fig. 6. Strength and engineering fracture strain data.

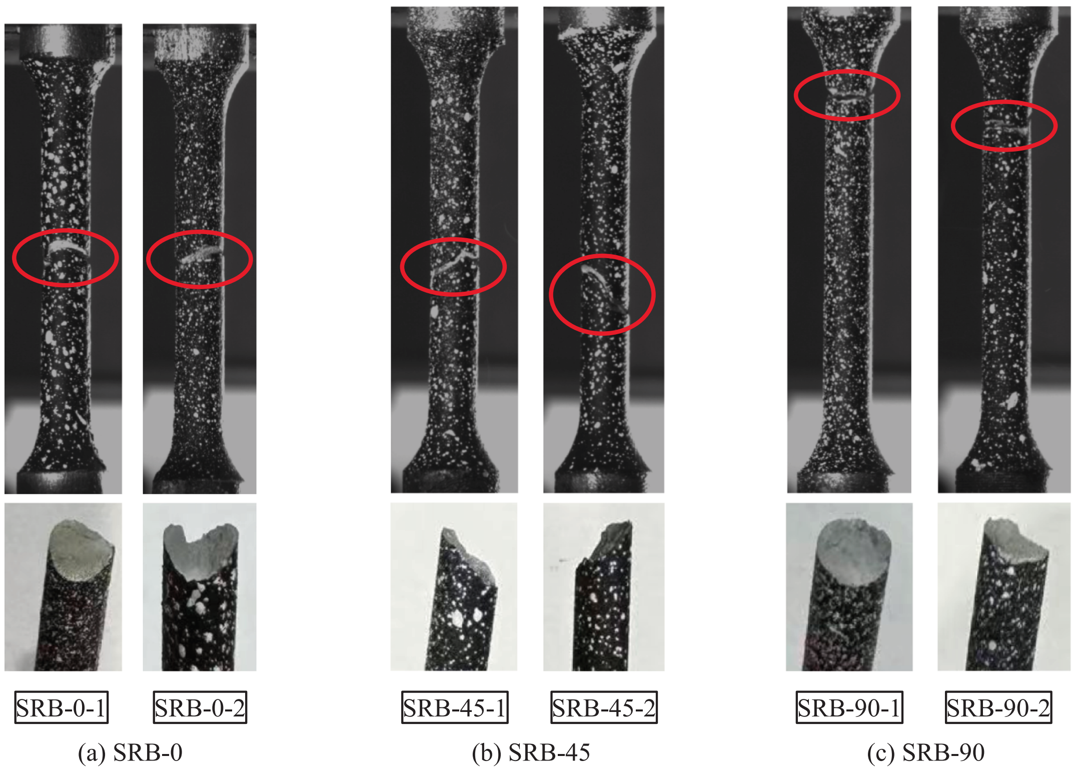

Fig. 7. Fracture profile of SRB specimens.

adjacent layers [35]. The lack of adhesion can be explained by the material shrinkage during cooling from high temperatures, which increases the number of internal defects between two adjacent layers.

The large discrepancy in ductility between the two SRB-90 specimens is likely due to variations in the density of these inter-layer defects. Since the quality of inter-layer bonding is not uniform, the extent of defects along the build direction can vary, resulting in noticeable differences in ductility. In contrast, the SRB-0 and SRB-45 specimens are loaded perpendicular to, or at 45° to, the build direction. Therefore, each cross-section intersects multiple printing layers, effectively averaging the influence of inter-layer defects across many printing layers. The averaging reduces the sensitivity of their ductility to local variations in defect density between two printing layers compared with the SRB-90 specimens.

2.3.2. Coupons for investigating fracture behaviour

Fig. 8 shows the load–displacement curves for all the fracture coupons, where anisotropic load–displacement responses are observed. Apparent differences in ductility are observed in the NRB-R20 and NRB-R6 specimens at two build direction angles, which may be explained as follows. First, the PBF-LB/M AlSi10Mg material may have anisotropic fracture properties. Second, variations of

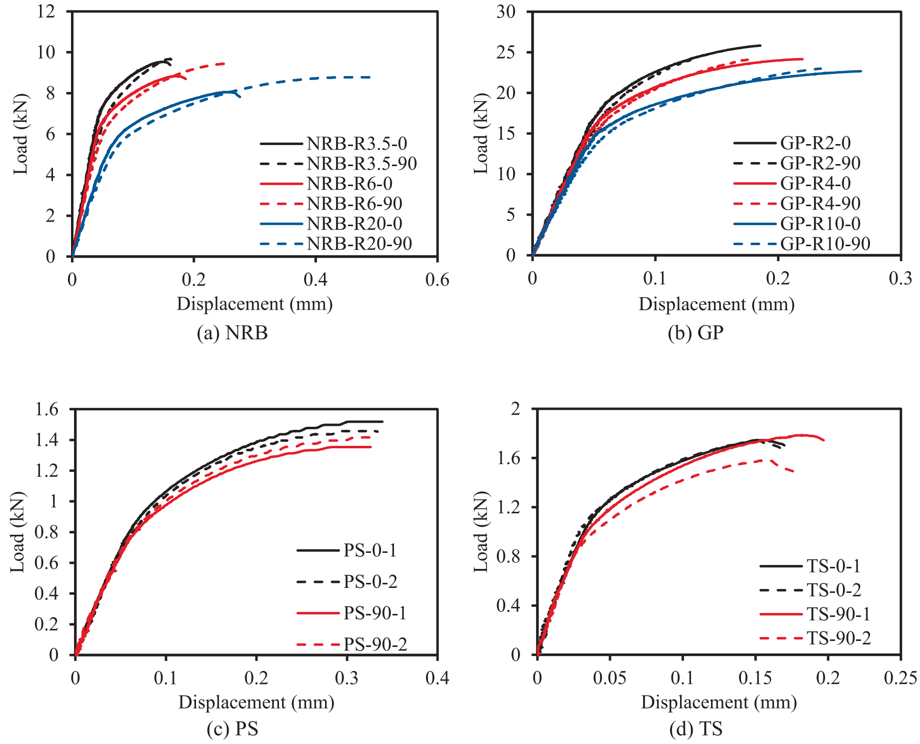

Fig. 8. Load-displacement curves for all fracture coupons.

defect density between layers, especially at $\theta = 90^{\circ}$, can lead to high variation in ductility for specimens of the same nominal configuration. The result from a single test may therefore not be representative of the material ductility under such a stress state. Third, as the stress state is affected by the constitutive behaviour [24], the mild anisotropy in the constitutive relationship shown in Section 2.3.1 may affect the stress state of fracture specimens with the same geometry but different build direction angles, in turn affecting the fracture strain and the resulting ductility in the load–displacement curve. The fracture properties in the two printing directions will be further analysed in Section 3.4 based on the values of stress triaxiality, Lode angle parameter and fracture strain extracted from finite element (FE) simulations of the tested specimens.

The load–displacement curves can be divided into two categories based on the fracture response: (1) fracture initiation followed by some propagation with increasing displacement until full fracture; and (2) fracture initiation with rapid propagation and the sudden entire loss of resistance. An example of the former category is NRB-R20-0, as shown in Fig. 9(a), while an example of the latter category is the specimen shown in Fig. 9(b). For both categories, the descending branches of the load–displacement curves are short or even absent, reflecting the rapid and unstable fracture propagation associated with the brittle nature of the material. For all specimens, except the PS and TS types, the stress state and plastic strain distributions have a low gradient across the fracture cross-sections [36]. Therefore, fracture initiates over a large area, leading to a marked reduction in specimen resistance, aligning with the observation of the curves in Category 1. The PS coupons show a sudden entire loss of resistance without observable softening, and are therefore classified as Category 2. The TS specimens, on the other hand, exhibit a relatively long fracture propagation range, rendering

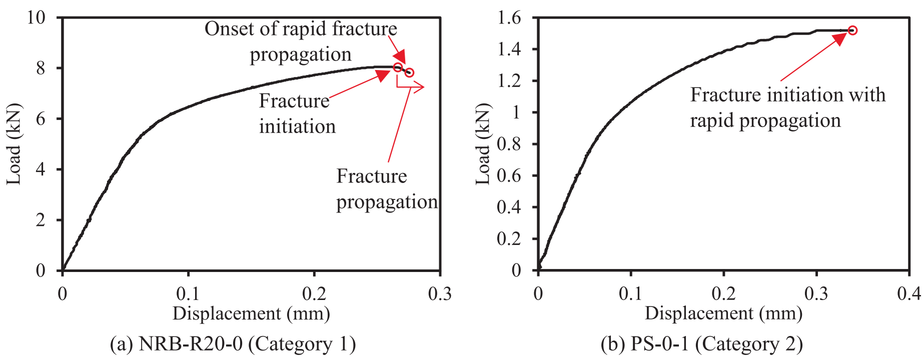

Fig. 9. Two different types of load–displacement curves based on fracture response.

identification of the exact fracture initiation displacement somewhat subjective. Hence, based on the analysis of the load–displacement curves, the displacements at fracture initiation Δ_f of all coupons, except the TS specimens, are presented in Table 4.

The fracture initiation location can sometimes be defined by analysing both the fracture surface and the DIC results. The fractured cross-section profiles of all SRBs are shown in Fig. 7, while those for all other coupons are shown in Fig. 10. Since the fracture profiles of the two repeated tests for each of the TS and PS specimens (in both build direction angles) are almost identical, only one representative profile is shown. Regarding the SRB specimens, necking is not apparent in any tests, indicating uniform stress and strain distributions across the entire cross-section. From void growth-coalescence based ductile fracture mechanics, fracture initiation depends on both the stress state and the equivalent plastic strain. The uniform distributions of both lead to approximately simultaneous fracture initiation across the entire cross-section for SRB specimens. In the case of suitably-designed NRB and GP specimens, fracture initiates at the centre of the cross-section [24]. As shown in Fig. 10(a-f), the cross-sections of all NRB and GP specimens displayed a typical cup-cone profile, featuring rough surfaces at the centre and smooth inclined surfaces at the edges. This typical profile indicates that fracture initiated at the centre of the cross-section for all specimens. Regarding the PS specimens, fracture initiation was not observed by the DIC system, i.e. it did not occur on the specimen surface, and the fracture profiles were relatively rough at the centres of the cross-sections. Both observations suggest that fracture initiated at the cross-section centre. Theoretically, PS specimens generate a pure shear stress state and have a uniformly smooth fracture surface. However, the observed roughness in the centre region is attributed to induced tensile stresses that develop after a certain degree of plastic deformation – the specimen rotates, and the shear surface is not perfectly aligned with the two pin supports, thereby inducing an additional tensile stress component at the cross-section centre [24]. For the TS specimens, fracture initiation could not be detected from the DIC measurements, indicating that failure initiated at a location other than the surface facing the DIC cameras. Accordingly, neither the fracture initiation displacement nor the initiation location can be reliably determined. Therefore, in Section 3, FE analysis for calibrating the material fracture properties is not performed for the TS specimens.

3. Finite element analysis

3.1. General

The fracture strains and stress states of all specimens cannot be directly obtained from the test observations, since most fractures initiated at the centre of the cross-section, as discussed in Section 2.3.2. Accordingly, parallel FE models were developed using the Abaqus software [37] to numerically track the developments of stress states and fracture strains in all specimens. The explicit solver was used in this study to avoid convergence problems.

In addition to the tested coupons, flat plate (FP) coupons from [13] were also modelled to expand the dataset. The FP specimens in [13] were manufactured using the same printing parameters and same batch of metallic powder as those used in the present study. As

Table 4
Key features of all coupons.

Coupon	Δ_f (mm)	Fracture initiation location	η_{av}	ξ_{av}	ε_f	ϕ
SRB-0–1	1.209	Whole cross-section	0.333	1.000	0.044	1.000
SRB-0–2	1.361	Whole cross-section				
SRB-45–1	1.016	Whole cross-section	0.333	1.000	0.035	1.000
SRB-45–2	1.076	Whole cross-section				
SRB-90–1	1.520	Whole cross-section	0.333	1.000	0.042	1.000
SRB-90–2	0.954	Whole cross-section				
NRB-R3.5–0	0.155	Cross-section centre	0.679	1.000	0.034	0.953
NRB-R3.5–90	0.163	Cross-section centre	0.650	1.000	0.033	1.000
NRB-R6-0	0.177	Cross-section centre	0.530	1.000	0.038	1.000
NRB-R6-90	0.255	Cross-section centre	0.535	1.000	0.060	1.000
NRB-R20-0	0.260	Cross-section centre	0.421	1.000	0.036	0.990
NRB-R20-90	0.503	Cross-section centre	0.434	1.000	0.096	1.000
GP-R2-0	0.182	Cross-section centre	0.934	0.198	0.026	0.840
GP-R2-90	0.132	Cross-section centre	0.831	0.541	0.018	0.950
GP-R4-0	0.220	Cross-section centre	0.752	−0.006	0.076	0.890
GP-R4-90	0.179	Cross-section centre	0.686	0.386	0.043	0.970
GP-R10-0	0.267	Cross-section centre	0.626	0.179	0.070	0.900
GP-R10-90	0.235	Cross-section centre	0.597	0.363	0.052	0.970
PS-0–1	0.339	Cross-section centre	0.025	0.078	0.110	1.000
PS-0–2	0.334	Cross-section centre				
PS-90–1	0.326	Cross-section centre	0.024	0.068	0.106	1.000
PS-90–2	0.334	Cross-section centre				
TS-0–1	—	Unknown	—	—	—	1.000
TS-0–2	—	Unknown	—	—	—	
TS-90–1	—	Unknown	—	—	—	1.000
TS-90–2	—	Unknown	—	—	—	
FP-0 [13]	1.92	Cross-section centre	0.333	1.000	0.047	1.000
FP-90 [13]	1.95	Cross-section centre	0.333	1.000	0.049	1.000

Fig. 10. Fracture profiles of NRB, GP, PS and TS specimens.

such, the printed material properties in [13] are regarded to be the same as those in the present study. There were 12 FP specimens in total with 6 oriented at $\theta = 0^\circ$ and 6 at $\theta = 90^\circ$. The detailed geometries and loading responses for these FP coupons can be found in [13].

3.2. Stress–strain relationship

3.2.1. Effect of stress state

The SRB specimens were used to calculate the stress–strain relationships. The engineering stress–strain curves shown in Fig. 4 were derived based on the initial geometries and gauge lengths of the specimens. However, in the FE modelling, the true stress–strain relationship is required to allow for the deformation of the specimens under load and hence to express the real material constitutive relationship. The following equations were used to calculate the true stress σ_{true} and true strain $\varepsilon_{\text{true}}$ before necking:

$$\sigma_{\text{true}} = \sigma_{\text{eng}}\left(1 + \varepsilon_{\text{eng}}\right) \tag{4}$$

$$\varepsilon_{\text{true}} = \ln\left(1 + \varepsilon_{\text{eng}}\right) \tag{5}$$

in which σ_{eng} is the engineering stress and ε_{eng} is the engineering strain.

Necking did not occur in any of the SRB specimens for all three build direction angles. Therefore, the constitutive relationships were determined using Eqs. (4) and (5) alone, without accounting for post-necking effects. However, the constitutive relationship obtained from the SRB specimens are valid only up to their fracture strains, which were relatively low compared to the other specimens. Therefore, it was necessary to extend the calibration of the constitutive relationship beyond the fracture strain of the SRB specimens using the other specimens with the highest fracture strains, i.e. the PS specimens in this study.

Since the constitutive relationship is affected by the stress state [38,39], careful consideration is required when combining calibration results from two different specimens subjected to distinct stress states. Specifically, the stress state is characterised by the stress triaxiality η and Lode angle parameter ξ. The constitutive relationship under different stress states can be represented by applying a stress correction factor ϕ to the reference constitutive relationship. In this study, the stress in the SRB specimens σ_{SRB} was used to define the reference constitutive curve. Accordingly, the stress in the constitutive relationship under any given stress state can be expressed as $\phi\ \sigma_{\mathrm{SRB}}$. Fig. 11 shows an example of a constitutive relationship calibration using the PS specimens. The simulation curve generated using the SRB-calibrated constitutive relationship with $\phi = 1$ shows good agreement with the experimental results. This consistency suggests that the constitutive relationship under $\eta = 1/3$ and $\xi = 1$ (associated with the SRB specimens) is similar to that under $\eta = 0$ and $\xi = 0$ (associated with the PS specimens), indicating that the influence of stress state on the constitutive behaviour is minimal under these two conditions. Therefore, the calibration of the constitutive relationship beyond the fracture strain of the SRB specimen can be based directly on the PS specimen data without applying any stress correction factor, i.e. by assuming $\phi = 1$.

Owing to the non-uniform stress and strain distribution across the critical cross-section in the PS specimens, the tested load–displacement curves cannot be directly converted into a stress–strain relationship. Therefore, the true stress–strain curve beyond the fracture strain of the SRB specimen was assumed to follow a predefined functional form with prespecified free model parameters. An iterative fitting process was then conducted to adjust the parameters until the best agreement with the test results was obtained. The proposed functional form is based on the second stage of the two-stage Ramberg-Osgood model [28,40], expressed as:

$$\varepsilon_{\mathrm{true}} = \frac{\sigma_{\mathrm{true}} - \sigma_{\mathrm{f,SRB}}}{E_{\mathrm{f,SRB}}} + \varepsilon_{\mathrm{a}}\left(\frac{\sigma_{\mathrm{true}} - \sigma_{\mathrm{f,SRB}}}{\sigma_{\mathrm{a}} - \sigma_{\mathrm{f,SRB}}}\right)^{b} + \varepsilon_{\mathrm{f,SRB}} \tag{6}$$

in which $\sigma_{\mathrm{f,SRB}}$ is the true stress of the SRB at fracture, $\varepsilon_{\mathrm{f,SRB}}$ is the true strain of the SRB at fracture, ε_{a} is any value of true strain which is larger than the highest fracture strain among all coupons, σ_{a} is the corresponding true stress and b is the free model parameter.

In this study, the chosen value of ε_{a} was 0.15, and the corresponding values of σ_{a} and b were calibrated through the iterative procedure described above. The calibrated values were found to be $\sigma_{\mathrm{a}} = 495$ MPa and $b = 7$ for the $\theta = 0^\circ$ specimens and $\sigma_{\mathrm{a}} = 475$ MPa and $b = 8$ for the $\theta = 90^\circ$ specimens. For the case of $\theta = 45^\circ$, only SRB specimens were tested; hence, the post-SRB fracture stress–strain relationship was assumed to follow a strain-hardening slope equal to that at the point of the fracture initiation of the SRB specimens. The resulting true stress–strain curves for all build direction angles under $\eta = 1/3$, $\xi = 1$ and $\eta = 0$, $\xi = 0$ are shown in Fig. 12. Note that, when calibrating the true stress–strain curves in each orientation, isotropic material behaviour was assumed.

The constitutive relationship, i.e. the value of ϕ, for each of the remaining coupons was analysed individually. For each specimen, the value of ϕ was assumed to remain constant throughout the plastic range. Several iterations were conducted until the best fit to the test curve was achieved. The final values for all specimens are given in Table 4. It can be seen that the coupons tested at $\theta = 0^\circ$ have a large variation in ϕ compared to those tested at $\theta = 90^\circ$, indicating a more pronounced effect of the stress state on the constitutive response at $\theta = 0^\circ$.

Notably, the GP specimens generally have lower ϕ values than the PS specimens, despite both designed to have zero average Lode angle parameters. This phenomenon is consistent with previous numerical observations [38,41,42] and is attributed to the distinct Lode angle parameter history, as shown in Fig. 13. The two coupons have clearly different Lode angle parameter histories: the GP specimen initially experiences high values of Lode angle parameter, which gradually decreases to zero with increasing plastic strain, while the PS specimen shows approximately zero Lode angle parameter at the onset of plasticity, which then increases with deformation. Based on these observations, for the material studied, the value of ϕ tends to be less than 1 when the Lode angle parameter is between 0 and 1. The initial high Lode angle parameter in the GP specimens reduces their resistance at the beginning of loading and continues to affect the response throughout deformation, indicating a lower value of ϕ in the early plastic range, where the Lode angle parameter is above zero. In contrast, as discussed previously, the PS specimens show $\phi = 1$ under pure shear conditions. This is attributed to the fact that, for the relatively low-ductility material tested in this study, the rotation of the critical region is insufficient to induce appreciable tensile stresses, allowing the specimen to remain close to a pure shear state throughout loading. However, for materials with higher ductility, large rotations develop during deformation, inducing significant tensile stresses in the critical region, thereby increasing the Lode angle parameter. This leads to a potential reduction in the value of ϕ. Correspondingly, FE simulations typically show good agreement with experiments ($\phi = 1$) in the early plastic range, followed by overestimations ($\phi < 1$) at larger plastic strains due to the increases in both stress triaxiality and Lode angle parameter. This behaviour explains the commonly observed

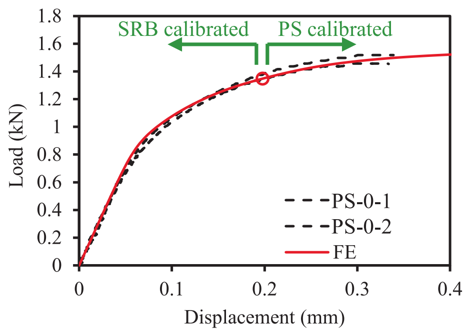

Fig. 11. Result of constitutive relationship calibration using PS specimens.

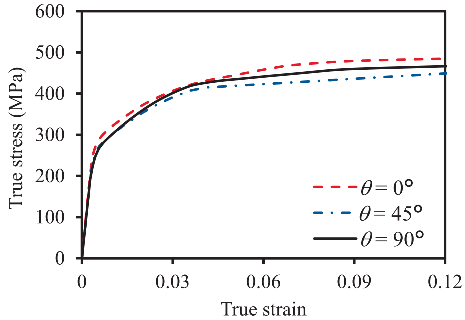

Fig. 12. True stress–strain curves under $\eta = 1/3$, $\xi = 1$ and $\eta = 0$, $\xi = 0$.

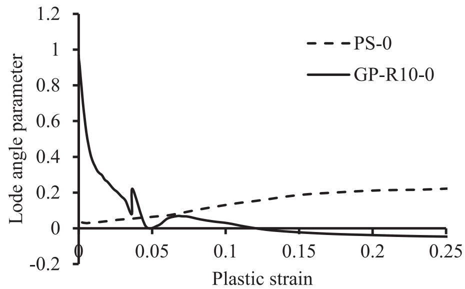

Fig. 13. Lode angle parameter histories of grooved plate (GP) and pure shear (PS) specimens.

overestimation of numerical responses in the later stages of loading for PS specimens, as reported in [42–44]. Note that the effect of stress triaxiality on ϕ is not considered in this analysis, as its influence is significantly lower compared to that of the Lode angle parameter [38].

The stress state and fracture strain of each specimen vary depending on whether the corrected or uncorrected constitutive relationship is applied. Fig. 14 shows an example using the GP-R4-0 specimen, in which the stress triaxiality from the simulation after correction is slightly higher than that before correction. A detailed comparison of the average stress state and fracture strain for each specimen, based on both the stress state-corrected (through ϕ) and −uncorrected constitutive relationships, is shown in Fig. 15. Note that the calculation of the average stress state and the method of extracting the stress state and fracture strain will be introduced in Section 3.4. While the stress triaxiality and fracture strain remain relatively consistent, a more notable discrepancy is observed in the Lode angle parameter, particularly for the GP specimens. The discrepancy is attributed to the sensitivity of the Lode angle parameter to the constitutive properties at the early stages of plastic deformation. It can be expected that, for high ductility materials, the Lode angle parameter will converge to zero regardless of whether the stress state-corrected or −uncorrected constitutive relationship is used. Accordingly, the predicted stress state and fracture strain for high ductility materials will be similar for simulations using either set of material properties. Note that the anisotropic constitutive properties are considered when calculating the stress states and fracture strains. The detailed method of considering the material anisotropy will be introduced in the next section.

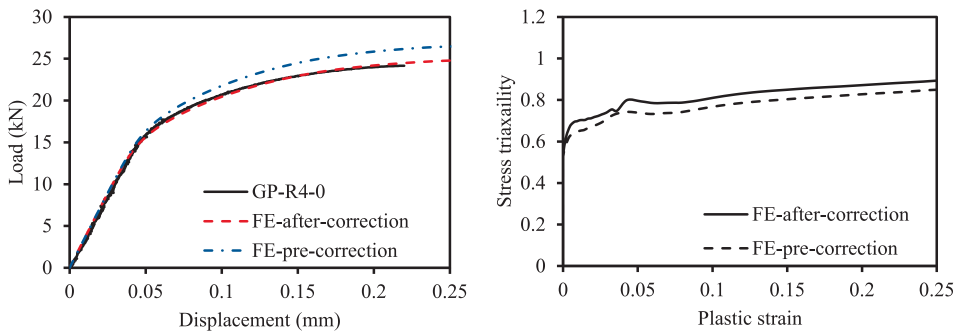

(a) Load-displacement curve (b) Stress triaxiality development

Fig. 14. FE simulation of GP-R4-0 using constitutive relationships before and after correction through the application of the parameter ϕ.

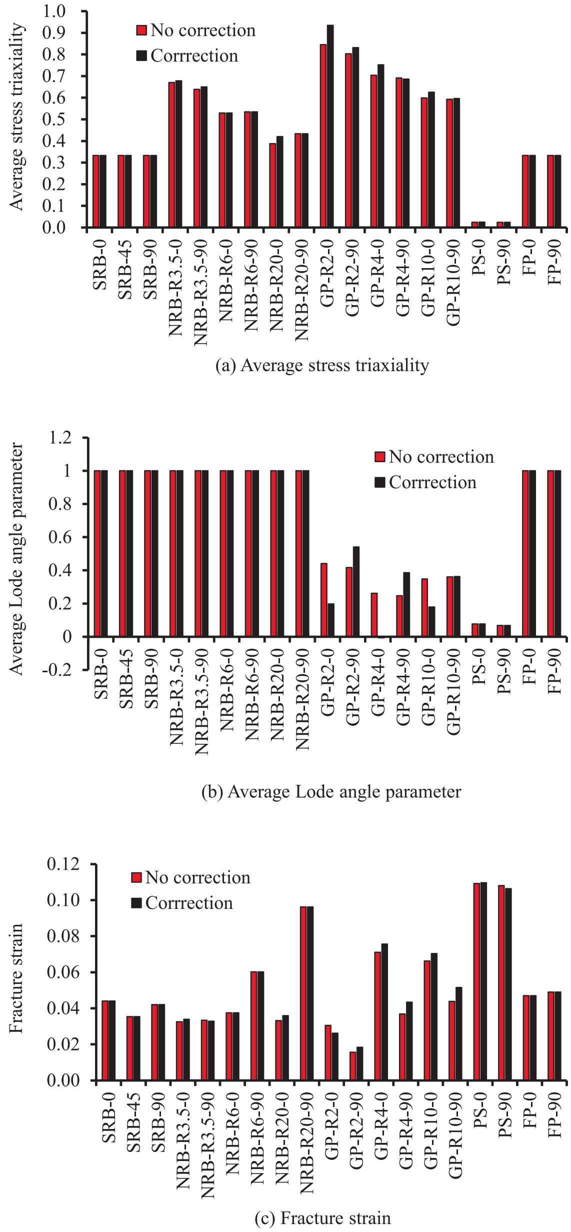

Fig. 15. Comparisons of stress state and fracture strain before and after the stress state correction of the constitutive relationship.

3.2.2. *Effect of material anisotropy*

Material anisotropy was observed in the tested material, as described in Section 2.3.1. Distinct constitutive relationships were therefore defined for each build direction angle. The anisotropic material model developed in [23] is adopted in this study. The model assumes transversely isotropic behaviour, which is suitable for the layer-wise PBF-LB/M material examined here. Owing to the rotating scan strategy adopted during specimen fabrication, the material properties can be reasonably assumed to be isotropic within the deposition plane (perpendicular to the build direction) at the macro-scale [15], indicating that the plane of transverse isotropy coincides with the deposition plane. In the elastic range, the relationship between the stress and strain tensors can be expressed using Hooke's Law, expressed as [23]:

$$\{\varepsilon\} = [S]\{\sigma\} \tag{7}$$

where $\{\sigma\} = [\sigma_{11}, \sigma_{22}, \sigma_{33}, \sigma_{12}, \sigma_{23}, \sigma_{31}]^{\mathrm{T}}$ is the stress tensor matrix, $\{\varepsilon\} = [\varepsilon_{11}, \varepsilon_{22}, \varepsilon_{33}, 2\varepsilon_{12}, 2\varepsilon_{23}, 2\varepsilon_{31}]^{\mathrm{T}}$ is the strain tensor matrix, and $[S]$ is elastic compliance tensor matrix. For transversely isotropic material, $[S]$ is giving by:

$$[S]=\begin{bmatrix} 1/E_0 & -\nu_p/E_0 & -\nu_{np}/E_{90} & & & \\ -\nu_p/E_0 & 1/E_0 & -\nu_{np}/E_{90} & & & \\ -\nu_{np}/E_{90} & -\nu_{np}/E_{90} & 1/E_{90} & & & \\ & & & 2(1+\nu_p)/E_0 & & \\ & & & & 1/G_{np} & \\ & & & & & 1/G_{np} \end{bmatrix} \tag{8}$$

where E_0 and E_{90} are the Young's moduli measured for specimens with $\theta = 0^\circ$ and $\theta = 90^\circ$, respectively, ν_p is the Poisson's ratio in the transversely isotropic plane, ν_{np} is the Poisson's ratio related to the normal and in-plane directions when the stress is applied in the 3-direction ($\theta = 90^\circ$), and G_{np} is the shear modulus related to the normal and in-plane directions.

In the plastic range, the Hill Yld48 criterion [45] was adopted in [23], featuring a quadratic formulation and six free model parameters, as given by:

$$f(\sigma)=\sqrt{\begin{matrix}F(\sigma_{22}-\sigma_{33})^2+G(\sigma_{33}-\sigma_{11})^2+H(\sigma_{11}-\sigma_{22})^2\\ +2L\sigma_{23}^2+2M\sigma_{31}^2+2N\sigma_{12}^2\end{matrix}}-\sigma_{r0} \tag{9}$$

where σ_{r0} is the initial reference true yield stress which is regarded as the true yield stress in the case of $\theta = 0^\circ$ in this study, and F, G, H, L, M and N are free model parameters. The calibration method considered the continuous variation of all six free model parameters throughout the entire plastic range, and the detailed calibration procedure can be found in [23].

The anisotropic material model in [23] requires coupon tests in three build direction angles to calibrate the model parameters. Hence, the three stress–strain curves in Fig. 12 are used for this calibration. The implementation of the anisotropic model was conducted via the Abaqus subroutine VUMAT [37], using the formulation provided in [23]. In the modelling, the values of ϕ were assigned for both build direction angles ($\theta = 0^\circ$ and $\theta = 90^\circ$) based on the calibration results corresponding to the specific specimen geometry; for example, $\phi = 0.90$ for GP-R10-0 and $\phi = 0.97$ for GP-R10-90. For the build direction angle at $\theta = 45^\circ$, where no corresponding coupon tests were conducted, ϕ was assumed to be 1 for all specimens.

The assignment of anisotropic material properties is necessary in order to capture the localised stress and strain distributions, and hence the stress state. This is demonstrated in Fig. 16 for the example case of the NRB-R6-0 specimen. The FE models using both anisotropic and isotropic mechanical behaviour produce comparable load–displacement curves, but the stress triaxiality determined using the anisotropic model is approximately 20% lower than that using the isotropic model, indicating the importance of incorporating anisotropic constitutive properties into the FE simulations.

3.3. FE model

Fig. 17 shows the FE model for each coupon type. For all coupons, three-dimensional solid elements with reduced integration (C3D8R) were used. Geometric symmetry was utilised to reduce the computational cost: for the PS and TS specimens, half of the coupons were modelled, while for the SRB, NRB, FP and GP specimens, one eighth of the coupons were modelled. The loading applied during the tests was simulated by a longitudinal displacement (Δ) at the coupon ends, reflecting the actual displacement-controlled loading protocol in the tests.

The critical fracture area was assigned a more refined mesh size relative to the remainder of the specimens, marked by red boxes in Fig. 17. The mesh size of each specimen was chosen based on the recommendations in [24], in which a detailed mesh sensitivity analysis was conducted for each coupon type. The FE model of each coupon employed the measured geometry, as given in Table 2. For specimens with repeated tests, the average values were used.

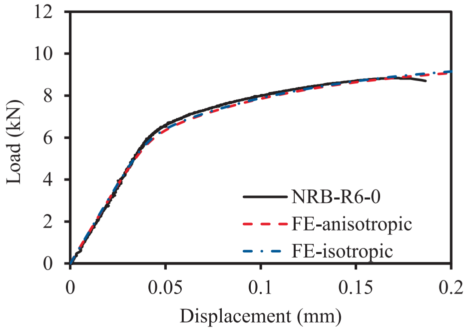

(a) Load-displacement curve

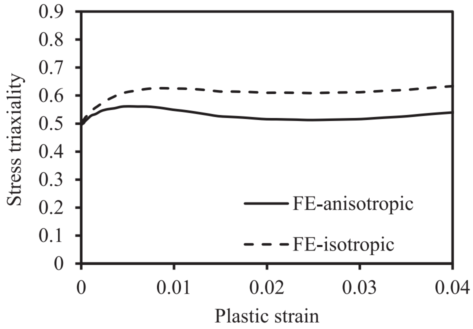

(b) Stress triaxiality development

Fig. 16. FE simulation of NRB-R6-0 with isotropic and anisotropic material properties.

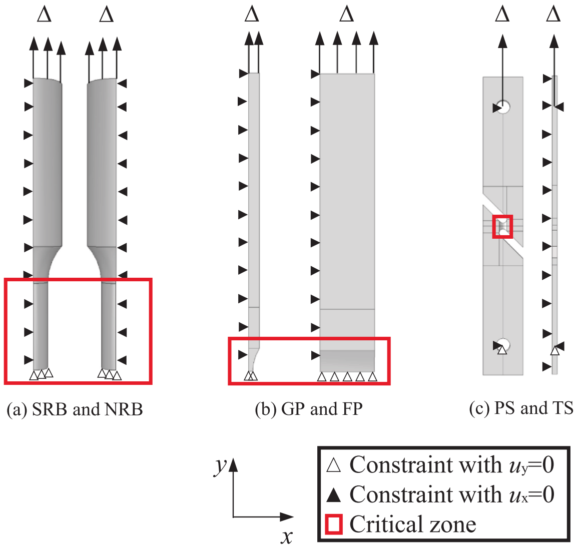

Fig. 17. FE model of each coupon type.

3.4. FE modelling results and fracture property analysis

The FE load–displacement curves for all specimens are plotted in Fig. 18. The curves with the anisotropic material behaviour differed only slightly from those idealised with the isotropic assumption, since the degree of anisotropy in the studied PBF-LB/M aluminium is relatively low. Overall, the simulation results show good agreement with the experimental results and are thus considered reliable for analysing the fracture properties of the tested PBF-LB/M aluminium.

For most coupons, η and ξ varied with the degree of plastic deformation, and hence their average values were employed in the fracture analysis to reflect the loading history. The average stress triaxiality η_{av} and Lode angle parameter ξ_{av} values were calculated as:

$$\eta_{av} = \frac{\int_0^{\varepsilon_f} \eta \, d\varepsilon_p}{\varepsilon_f} \text{ and } \xi_{av} = \frac{\int_0^{\varepsilon_f} \xi \, d\varepsilon_p}{\varepsilon_f} \tag{10}$$

in which ε_f is the plastic equivalent strain at fracture initiation (referred to as the fracture strain) and ε_p is the plastic strain.

The average stress state (η_{av} and ξ_{av}) and fracture strain (ε_f) for each coupon were extracted from the corresponding FE simulation results. These three parameters were determined from the element located at the fracture initiation location and at the displacement corresponding to fracture initiation Δ_f. The relevant data are summarised in Table 4 for all specimens, except the TS specimens, where the fracture initiation location was difficult to determine reliably, and any misidentification of the location could lead to significant inaccuracies in the calibration of the fracture models.

Fig. 19 shows the fracture strains for each specimen type, where $\xi_{av} = 1$ for the SRB, NRB and FP specimens, and $\xi_{av} \approx 0$ for the GP and PS specimens. Note that the red crosses in Fig. 19 do not strictly represent fracture strains under $\xi_{av} = 0$, since most GP specimens have ξ_{av} values larger than 0. As shown in Fig. 19(a), for specimens tested at the 0° build direction angle, the fracture strains generally follow the theoretical exponential trend with stress triaxiality. In contrast, Fig. 19(b) shows that for the specimens tested at $\theta = 90°$, the maximum fracture strain occurs at a η_{av} value of 0.434, rather than at 1/3 for $\xi_{av} = 1$, as predicted by theory. Notably, the SRB and FP specimens both generate the same stress state ($\eta_{av} = 1/3$ and $\xi_{av} = 1$) and show nearly consistent fracture strains. Given that there are eight tests in total for SRB-90 and FP-90, but only one test for NRB-R20-90 and NRB-R6-90, the fracture strain at $\eta_{av} = 1/3$ and $\xi_{av} = 1$ is considered to be more reliable than those at the higher η_{av} values. The high fracture strains observed at high η_{av}-values may be attributed to a low defect density, due to particularly good adhesion between adjacent printing layers, as discussed in Section 2.3.1. The defect density varies across melt pool boundaries, which are considered to be the primary cause of the scatter in the data and the inconsistencies in ductility among repeated tests for a given coupon configuration. This effect is especially pronounced in the NRB specimens at $\theta = 90°$, which consistently fail at the minimum cross-section containing only one melt pool boundary, thereby leading to the deviations of fracture strain from the theoretical predictions.

Fig. 19(c) compares the fracture strain data across both build direction angles. In general, the fracture strains between the two build direction angles are consistent for most specimens, including the SRB, FP, PS and NRB-R3.5 specimens. However, outliers are observed for NRB-R20 and NRB-R6, which show noticeably higher fracture strains at $\theta = 90°$. The considerably higher fracture strains for these two specimens are attributed to particularly good adhesion between the print layers near the minimum cross-section, resulting in reduced defect density and therefore enhanced ductility. Note that the GP specimens are excluded in this comparison due to their differing average Lode angle parameters.

In this study, two fracture criteria were calibrated and their ability to predict the true fracture strain of the specimens under the distinct stress states were compared: the Positive Stress Triaxiality-Lode Angle Parameter Interaction Model (PTLIM) criterion [34],

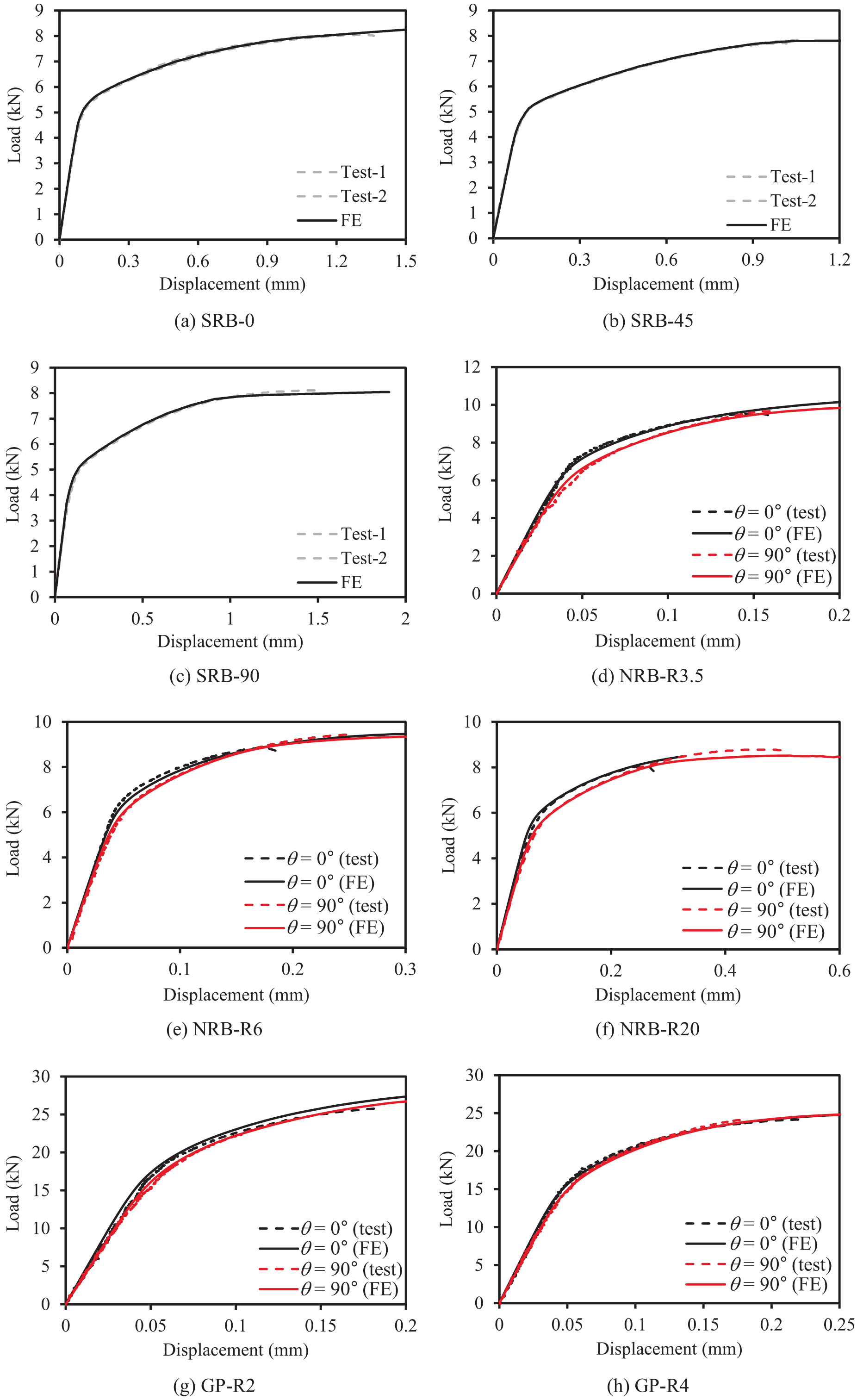

Fig. 18. Comparison between test and FE modelling results.

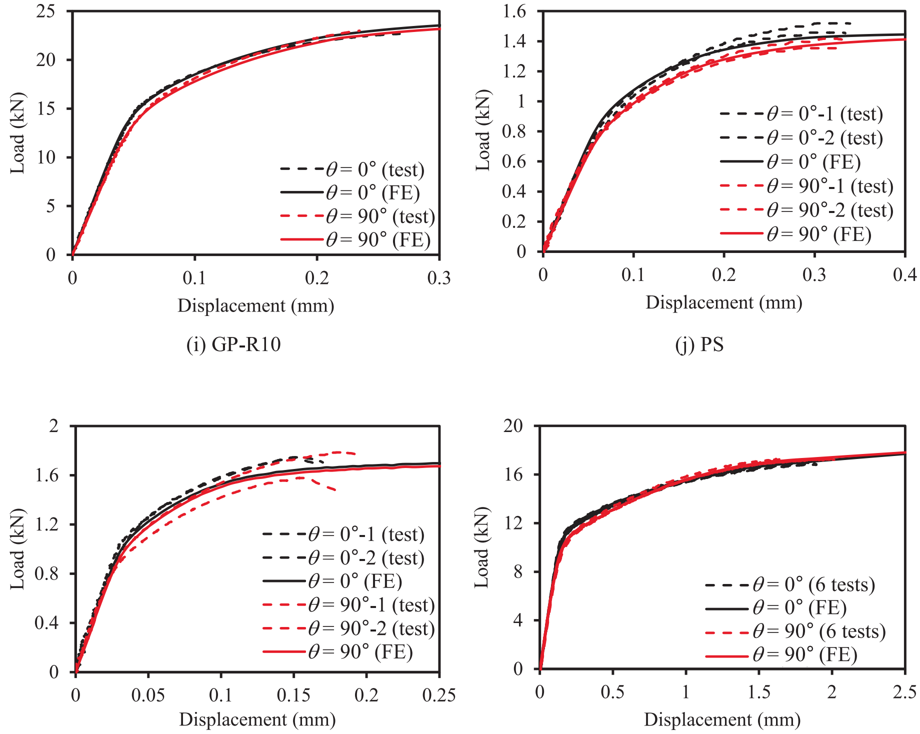

(i) GP-R10 (j) PS

(k) TS (l) FP

Fig. 18. (*continued*).

which considers the interaction effects of stress triaxiality and Lode angle parameter on the fracture strain; and the Lode Angle Modified Void Growth Method (LMVGM) criterion [46], which incorporates both effects of stress triaxiality and Lode angle parameter individually. The integral form of the PTLIM is expressed as:

$$D = \alpha_{\mathrm{PTLIM}} \int_0^{\varepsilon_\mathrm{f}} e^{\beta_{\mathrm{PTLIM}}\eta\left(\xi^2+1\right)^{\gamma_{\mathrm{PTLIM}}}} d\varepsilon_\mathrm{p} \tag{11}$$

in which α_{PTLIM}, β_{PTLIM} and γ_{PTLIM} are the free model parameters, and D is the damage index; fracture initiates when $\int dD = 1$.

When the stress state remains constant throughout the loading process, the PTLIM can be expressed as:

$$\varepsilon_\mathrm{f} = \frac{1}{\alpha_{\mathrm{PTLIM}}} e^{-\beta_{\mathrm{PTLIM}}\eta\left(\xi^2+1\right)^{\gamma_{\mathrm{PTLIM}}}} \tag{12}$$

The LMVGM incorporates the effects of stress triaxiality and Lode angle parameters on fracture using exponential functions. The integral form of LMVGM is defined as:

$$D = \alpha_{\mathrm{LMVGM}} \int_0^{\varepsilon_\mathrm{f}} e^{\beta_{\mathrm{LMVGM}}\eta - \gamma_{\mathrm{LMVGM}}\xi} d\varepsilon_\mathrm{p} \tag{13}$$

where α_{LMVGM}, β_{LMVGM} and γ_{LMVGM} are the free model parameters.

When the stress state remains constant throughout the loading process, the LMVGM is expressed by:

$$\varepsilon_\mathrm{f} = \frac{1}{\alpha_{\mathrm{LMVGM}}} e^{-\beta_{\mathrm{LMVGM}}\eta + \gamma_{\mathrm{LMVGM}}\xi} \tag{14}$$

Both fracture criteria are calibrated by minimising the Root Mean Squared Relative Error (RMSRE), which is defined as:

$$\mathrm{RMSRE} = \sqrt{\frac{\sum_{\mathrm{i}=1}^{N}\left(\frac{\varepsilon_{\mathrm{ft}}-\varepsilon_{\mathrm{fp}}}{\varepsilon_{\mathrm{ft}}}\right)_\mathrm{i}^2}{N}} \times 100\% \tag{15}$$

where N is the total number of coupon types, $\varepsilon_{\mathrm{ft}}$ is the tested fracture strain, and $\varepsilon_{\mathrm{fp}}$ is the predicted fracture strain.

Given the observed anisotropic fracture behaviour, the free model parameters are first calibrated independently for each build direction angle. Then, a unified set of parameters is calibrated across both orientations, as given in Table 5. The corresponding

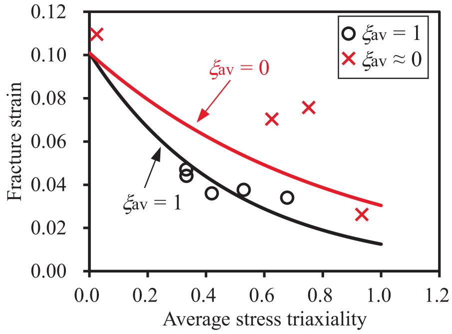

(a) Data and calibration at $\theta = 0°$

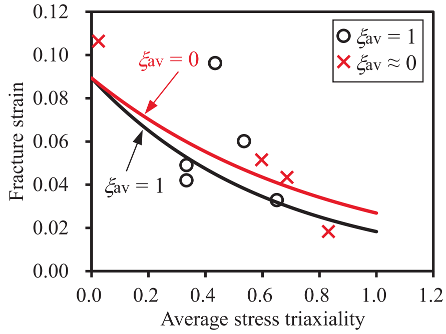

(b) Data and calibration at $\theta = 90°$

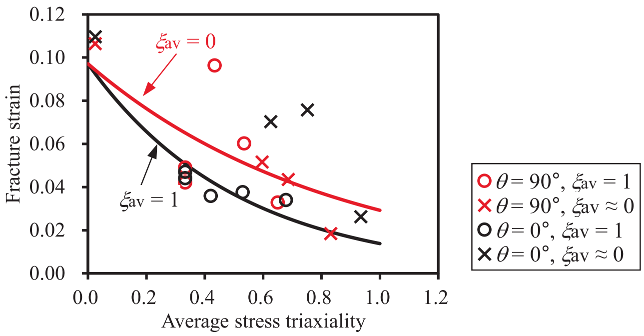

(c) Data and calibration for both material orientation

Fig. 19. Fracture strains at different stress states for data and calibrated PTLIM curve at (a) $\theta = 0°$, (b) $\theta = 90°$ and (c) $\theta = 0°$ and $\theta = 90°$.

Table 5
Calibrated fracture free model parameters.

Calibration using the data at the build direction angle (°)	PTLIM				LMVGM			
	α_{PTLIM}	β_{PTLIM}	γ_{PTLIM}	RMSRE	α_{LMVGM}	β_{LMVGM}	γ_{LMVGM}	RMSRE
0	9.9	1.2	0.8	0.241	9.3	1.0	−0.6	0.211
90	11.2	1.2	0.4	0.318	10.4	1.1	−0.4	0.341
			All	0.282				0.283
0 and 90	10.3	1.2	0.7	0.289	8.9	1.2	−0.7	0.303

prediction curves of the PTLIM, generated using the free model parameters for the individual ($\theta = 0°$ and $\theta = 90°$) and both build direction angles, are shown in Fig. 19(a, b) and Fig. 19(c), respectively. The lower RMSRE values for the $\theta = 0°$ specimens relative to the $\theta = 90°$ specimens indicate higher consistency in the results when the loading is applied in the $\theta = 0°$ direction, corroborating the earlier observations.

The RMSRE calculated using all calibrated free model parameters are summarised in Table 5. Overall, the RMSRE obtained from the parameters calibrated using all data points are comparable for the PTLIM and LMVGM (0.289 vs 0.303), showing a similar level of accuracy in predicting the fracture strain of the tested PBF-LB/M aluminium. The calibrated parameters related to stress triaxiality (β_{PTLIM} and β_{LMVGM}) are almost the same between build direction angles, suggesting a similar void growth ratio for a given stress state. In contrast, larger differences are observed in the other parameters between the two build directions. This is attributed to the combined influence of defect density variations and the anisotropic constitutive response on the fracture behaviour.

The RMSRE values obtained using two build direction angle-specific sets of free model parameters are slightly lower than those using the unified free model parameter – see Table 5. This indicates that the difference between the anisotropic fracture properties in the two build direction angles is relatively minor. The observed variations in the load–displacement curves in Fig. 8 are therefore mainly attributed to the variation in interlayer adhesion (defect density), rather than differences in the fracture behaviour itself.

Fig. 20 shows examples of load–displacement curves and fracture simulations obtained from the FE models incorporating the PTLIM (with the unified model parameters), compared to the experiment results, including one representative specimen from each coupon type (SRB, NRB, GP and PS) in both build direction angles. Various methods are available for predicting fracture, including the cohesive zone method [47] and the extended finite element method [48], the element deletion method [37] and the phase field method

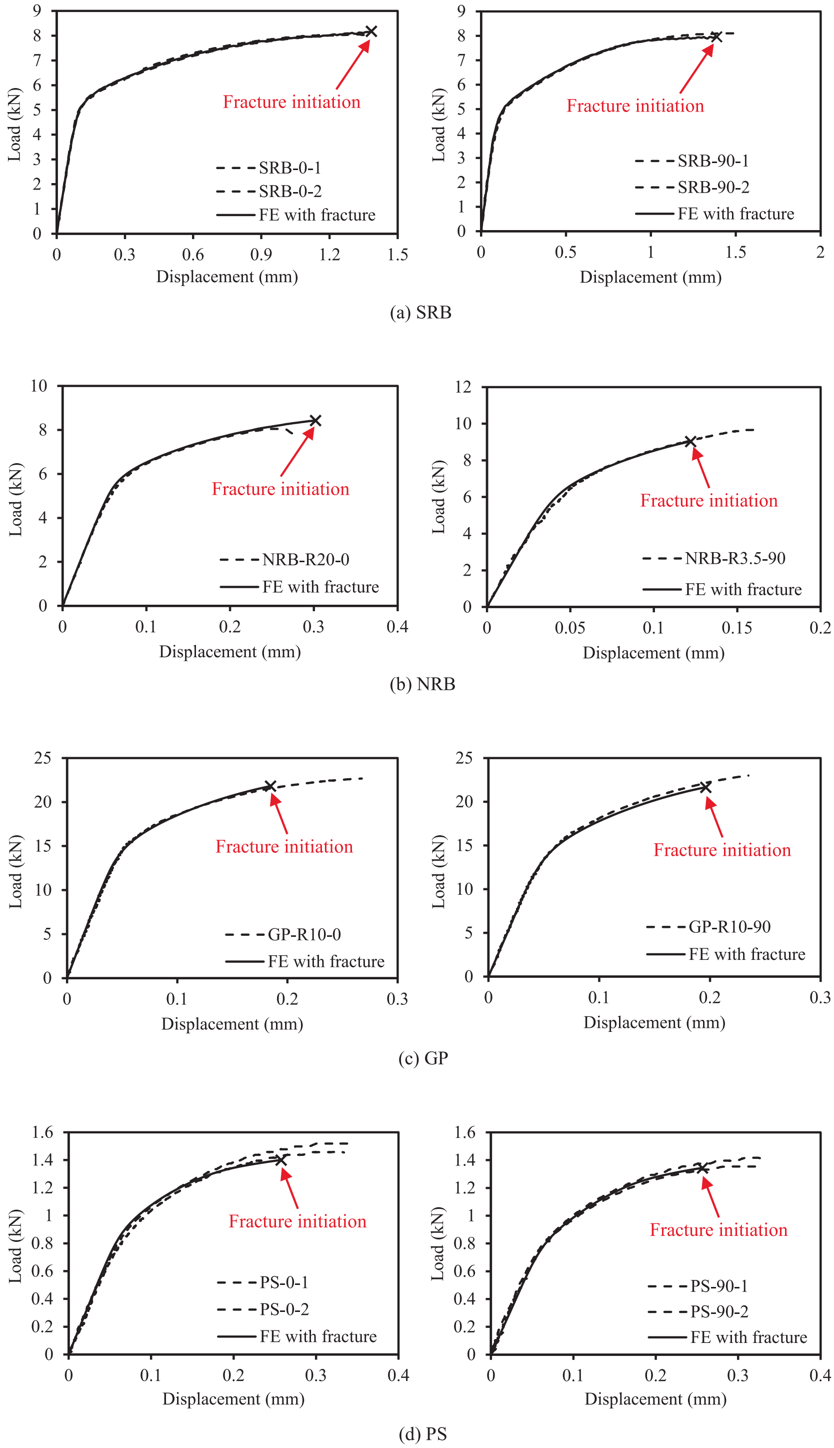

Fig. 20. Fracture simulation results compared with experiments for (a) SRB, (b) NRB, (c) GP and (d) PS specimens.

[49]. The element deletion method is conceptually simple and can provide accurate predictions when sufficient mesh refinement is applied along the fracture path; therefore, it is adopted in the present study. The method consists of removing elements once the stress state (η, ξ) and plastic strain history satisfy the fracture initiation criterion. Owing to the low gradients of stress state and plastic strain at the critical cross-sections of all coupons, fracture in the simulations initiated over a relatively wide region, leading to a significant reduction in resistance. Rapid fracture propagation was then observed, as complete fracture occurred almost simultaneously with fracture initiation. Therefore, only the fracture initiation points are indicated in Fig. 20. Overall, the FE simulations are in good

agreement with the experimental results. However, certain cases, such as GP-R10-0, show relatively high discrepancies, which are attributed to the inherent limitations in the calibrated free model parameters. While the unified parameter set achieves high overall accuracy, it may compromise the accuracy for some specimens.

4. Conclusions

The constitutive and fracture behaviour of additively manufactured AlSi10Mg aluminium alloy printed by laser beam powder bed fusion (PBF-LB/M) has been investigated in this paper. A total of 26 coupons with nine different configurations were designed and tested under various stress states and build direction angles. Parallel FE models were developed to investigate the effects of stress state and build direction angle on the fracture behaviour. In the FE simulations, both the stress state-dependent softening of the constitutive response and anisotropic mechanical behaviour were incorporated to ensure accurate predictions of fracture strains under well-defined stress states. The present study focused on understanding the constitutive and fracture behaviour of PBF-LB/M aluminium under various stress states and build directions, supported by finite element simulations. However, the effects of microstructural features, including interlayer bonding quality and defect distributions, on the observed material and fracture behaviour were not explicitly characterised in this study and could be explored in future work. The following major conclusions were drawn:

(1) Mild anisotropic constitutive behaviour was observed, with the maximum Young's modulus and proof strengths occurring at $\theta = 0^\circ$.

(2) Two NRB specimens at $\theta = 90^\circ$ showed considerably higher fracture strains than the other specimens, attributed to particularly good interlayer adhesion near the critical cross-section, resulting in reduced defect density and therefore enhanced ductility.

(3) Except two outliers (NRB-R20 at $\theta = 90^\circ$ and NRB-R6 at $\theta = 90^\circ$), the fracture strains in the 0° and 90° build direction angles were found to be generally consistent, indicating minor anisotropy in fracture behaviour.

(4) Two ductile fracture criteria, namely the PTLIM and LMVGM, were calibrated and showed comparable predictive capabilities, with Root Mean Squared Relative Errors of 0.289 and 0.303, respectively.

CRediT authorship contribution statement

Jingsheng Zhou: Writing – original draft, Visualization, Validation, Software, Investigation, Formal analysis. **Ruizhi Zhang:** Writing – original draft, Visualization, Methodology, Investigation, Conceptualization. **Mohsen Amraei:** Software, Resources, Conceptualization. **Leroy Gardner:** Writing – review & editing, Supervision, Project administration, Funding acquisition, Conceptualization.

Declaration of competing interest

The authors declare that they have no known competing financial interests or personal relationships that could have appeared to influence the work reported in this paper.

Acknowledgements

The authors would like to thank University of Turku for providing the test specimens and Paul Crudge and Freddy Olivo at Imperial College London for their assistance in the experimental programme.

Data availability

Data will be made available on request.

References

[1] Gardner L. Metal additive manufacturing in structural engineering – review, advances, opportunities and outlook. Structures 2023;47:2178–93.
[2] Meng X, Gardner L. Standardisation framework for metal additive manufacturing in construction. Autom Constr 2025;176:106267.
[3] Afkhami S, Amraei M, Gardner L, Piili H, Wadee MA, Salminen A, et al. Mechanical performance and design optimisation of metal honeycombs fabricated by laser powder bed fusion. Thin-Walled Struct 2022;180:109864.
[4] Meng X, Weber B, Nitawaki M, Gardner L. Optimisation and testing of wire arc additively manufactured steel stub columns. Thin-Walled Struct 2023;189: 110857.
[5] Guo X, Kyvelou P, Ye J, Teh LH, Gardner L. Experimental investigation of wire arc additively manufactured steel single-lap shear bolted connections. Thin-Walled Struct 2022;181:110029.
[6] Weber B, Meng X, Gardner L. Optimised and 3D printed steel garden bridge: from design to experimental verification. Autom Constr 2026;181:106638.
[7] Yang J, Wadee MA, Gardner L. Strengthening of steel I-section beams by wire arc additive manufacturing — Concept and experiments. Engng Struct 2025;322: 119113.
[8] Yang J, Wadee MA, Gardner L. Strengthening of hot-rolled S355 steel I-section beams using WAAM high strength steel. Thin-Walled Struct 2025;215:113437.
[9] Liu J, Li G, Li C, Li C, Fang J. Plasticity and fracture properties of laser powder bed fusion fabricated 316L stainless steel - Experimental and numerical investigations. Mech Mater 2026;215:105597.
[10] Wilson-Heid AE, Qin S, Beese AM. Multiaxial plasticity and fracture behavior of stainless steel 316L by laser powder bed fusion: Experiments and computational modeling. Acta Mater 2020;199:578–92.
[11] Larrosa NO, Wang W, Read N, Loretto MH, Evans C, Carr J, et al. Linking microstructure and processing defects to mechanical properties of selectively laser melted AlSi10Mg alloy. Theor Appl Fract Mech 2018;98:123–33.

[12] Del Guercio G, McCartney DG, Aboulkhair NT, Robertson S, Maclachlan R, Tuck C, et al. Cracking behaviour of high-strength AA2024 aluminium alloy produced by Laser Powder Bed Fusion. Addit Manuf 2022;54:102776.
[13] Zhang R, Amraei M, Piili H, Gardner L. Testing of additively manufactured aluminium material and cross-sections in compression. Engng Struct 2025;341:120798.
[14] Paul MJ, Liu Q, Best JP, Li X, Kruzic JJ, Ramamurty U, et al. Fracture resistance of AlSi10Mg fabricated by laser powder bed fusion. Acta Mater 2021;211:116869.
[15] Weaver JS, Rosenthal I. Understanding Anisotropic Tensile Properties of Laser Powder Bed Fusion Additive Metals - Detailed Review of Select examples. Targeted News Service, Washington, D.C.: Targeted News Service; 2021.
[16] Zhao L, Santos Macías JG, Douillard T, Li Z, Simar A. Unveiling damage sites and fracture path in laser powder bed fusion AlSi10Mg: Comparison between horizontal and vertical loading directions. Materials Science and Engineering A, Structural Materials : Properties, Microstructure and Processing 2021;807:140845.
[17] Yan Q, Song B, Shi Y. Comparative study of performance comparison of AlSi10Mg alloy prepared by selective laser melting and casting. J Mater Sci Technol 2020;41:199–208.
[18] Tradowsky U, White J, Ward RM, Read N, Reimers W, Attallah MM. Selective laser melting of AlSi10Mg: Influence of post-processing on the microstructural and tensile properties development. Mater Des 2016;105:212–22.
[19] Zhang R, Amraei M, Piili H, Gardner L. Microstructure, mechanical properties and cross-sectional behaviour of additively manufactured stainless steel cylindrical shells. Thin-Walled Struct 2025;208:112750.
[20] Zhang R, Gardner L, Amraei M, Buchanan C, Piili H. Testing and analysis of additively manufactured stainless steel corrugated cylindrical shells in compression. J Engng Mech 2023;149(4).
[21] Zhang R, Meng X, Gardner L. Shape optimisation of stainless steel corrugated cylindrical shells for additive manufacturing. Engng Struct 2022;270:114857.
[22] BS En ISO. 6892-1, Metallic materials – Tensile testing – Part 1: Method of test at ambient temperature British Standard. Brussels: CEN; 2009.
[23] J. Zhou, R. Zhang, L. Gardner, Three-dimentional anisotropic mechanical model for additively manufactured metals (In preparation).
[24] Zhou J, Yan S, Rasmussen KJR, Zhang M. Test-and-FE-based method for obtaining complete stress-strain curves of structural steels including fracture. J Constr Steel Res 2025;25:109095.
[25] Meng X, Gardner L. Behavior and design of normal- and high-strength steel SHS and RHS columns. J Struct Engng 2020;146(11).
[26] LaVision Inc. Davis 10(2), 2021.
[27] Ramberg W, Osgood W. Determination of stress–strain curves by three parameters. National Advisory Committee on Aeronautics (NACA) 1941.
[28] Rasmussen KJR. Full-range stress–strain curves for stainless steel alloys. J Constr Steel Res 2003;59(1):47–61.
[29] Yun X, Wang Z, Gardner L. Full-range stress–strain curves for aluminum alloys. J Struct Engng 2021;147(6).
[30] Huang Y, Young B. The art of coupon tests. J Constr Steel Res 2014;96:159–75.
[31] Hadadzadeh A, Shalchi Amirkhiz B, Odeshi A, Li J, Mohammadi M. Role of hierarchical microstructure of additively manufactured AlSi10Mg on dynamic loading behavior. Addit Manuf 2019;28:1–13.
[32] Tang M, Pistorius PC. Anisotropic mechanical behavior of AlSi10Mg parts produced by selective laser melting. JOM 2017;69(3):516–22.
[33] Rice JR, Tracey DM. On the ductile enlargement of voids in triaxial stress fields. J Mech Phys Solids 1969;17(3):201–17.
[34] Zhou J, Gardner L. New void growth-based ductile fracture models incorporating interaction effects of stress triaxiality and Lode angle parameter. Theor Appl Fract Mech 2025;140:105204.
[35] Spiller S, Razavi N. Quasi-static and fatigue behavior of 316L stainless steel produced via material extrusion additive manufacturing: Insights from subtracted small-scale specimens. Materials Science and Engineering A, Structural Materials: Properties, Microstructure and Processing 2025;938:148439.
[36] Smith CM, Deierlein GG, Kanvinde AM. A stress-weighted damage model for ductile fracture initiation in structural steel under cyclic loading and generalized stress states. Stanford University; 2014. PhD Thesis.
[37] D. Systèmes, Abaqus 6.14 Documentation. Version 6.14-4, Providence, RI, USA, www.simulia.com, 2014.
[38] Bai Y, Wierzbicki T. A new model of metal plasticity and fracture with pressure and Lode dependence. Int J Plast 2008;24(6):1071–96.
[39] Wang Y-Z, Li G-Q, Wang Y-B, Lyu Y-F, Li H. Ductile fracture of high strength steel under multi-axial loading. Engng Struct 2020;210:110401.
[40] Kucukler M, Xing Z, Gardner L. Behaviour and design of stainless steel I-section columns in fire. J Constr Steel Res 2020;165:105890.
[41] Zhou J, Yan S, Rasmussen KJR, Zhang H, Deierlein GG. Ductile fracture simulation of shear-out strength behaviour and design equations of bolted lap joints. J Struct Engng 2025;151(9):04025134.
[42] Zhou J, Yan S, Rasmussen KJR, Deierlein GG. Development and validation of a model to calculate full-range response of bolted angle cleats in bending. J Constr Steel Res 2025;228:109397.
[43] J. Zhou, S. Yan, K.J.R. Rasmussen, G.G. Deierlein, Numerical and theoretical analyses of the shear-out strength of single-bolt lap joints. 18th East Asia-Pacific Conference on Structural Engineering and Construction, Chiang Mai, Thailand, 2024.
[44] Yan S, Zhao X. A fracture criterion for fracture simulation of ductile metals based on micro-mechanisms. Theor Appl Fract Mech 2018;95:127–42.
[45] R. Hill, A theory of the yielding and plastic flow of anisotropic metals. Proceedings of the Royal Society of London. Series A, Mathematical and physical sciences, 193(1033) (1948) 281-297.
[46] Liu X, Yan S, Rasmussen KJR, Deierlein GG. Experimental investigation of the effect of Lode angle on fracture initiation of steels. Engng Fract Mech 2022;271:108637.
[47] Xia L, Shih CF. Ductile crack growth-I. a numerical study using computational cells with microstructurally-based length scales. J Mech Phys Solids 1995;43(2):233–59.
[48] Moës N, Dolbow J, Belytschko T. A finite element method for crack growth without remeshing. Int J Numer Meth Engng 1999;46(1):131–50.
[49] Li C, Liu J, Dong L, Wu C, Steven G, Li Q, et al. Phase field fracture in elastoplastic solids: a stress-state, strain-rate, and orientation dependent model in explicit dynamics and its applications to additively manufactured metals. J Mech Phys Solids 2025;197:105978.